Monolithic beam combined quantum cascade laser arrays with integrated arrayed waveguide gratings

TUSHAR SANJAY KARNIK,[1,3,†] **LAURENT DIEHL,**[2,4,†] **KHOI PHUONG DAO,**[1] **QINGYANG DU,**[1] **CHRISTIAN PFLÜGL,**[2] **DARYOOSH VAKHSHOORI,**[2] **AND JUEJUN HU**[1]

[1]*Department of Materials Science & Engineering, Massachusetts Institute of Technology, Cambridge, Massachusetts 02139, USA*

[2]*Pendar Technologies, LLC, Cambridge, Massachusetts 02138, USA*

[3]*tkarnik@mit.edu*

[4]*diehl@pendar.com*

[†]Contributed equally to this work.

Abstract: Quantum cascade lasers (QCLs) are ubiquitous mid-infrared sources owing to their flexible designs and compact footprints. Manufacturing multiwavelength QCL chips with high power levels and good beam quality is highly desirable for many applications. In this study, we demonstrate an $\lambda \sim 4.9\,\mu m$ monolithic, wavelength beam-combined (WBC) infrared laser source by integrating on a single chip array of five QCL gain sections with an arrayed waveguide grating (AWG). Optical feedback from the cleaved facets enables lasing, whereas the integrated AWG locks the emission spectrum of each gain section to its corresponding input channel wavelength and spatially combines their signals into a single-output waveguide. Our chip features high peak power from the common aperture exceeding 0.6 W for each input channel, with a side-mode suppression ratio (SMSR) of over 27 dB when operated in pulsed mode. Our active/passive integration approach allows for a seamless transition from the QCL ridges to the AWG without requiring regrowth or evanescent coupling schemes, leading to a robust design. These results pave the way for the development of highly compact mid-IR sources suitable for applications such as hyperspectral imaging.

1. Introduction

The development of mid-infrared laser sources is of significant importance for a wide range of applications, including free-space communication, hyperspectral imaging, laser surgery, and chemical sensing. Various lasers operating in the mid-infrared range have emerged to meet the demands of these applications, including rare-earth-doped gain media lasers [1,2], semiconductor lasers [3–5], and optical parametric oscillators (OPOs) [6,7]. Among these, quantum cascade lasers (QCLs) [8] have achieved remarkable success at wavelengths beyond ~3.5 μm, making them the technology of choice for applications that require versatile, compact, and affordable laser sources. The performance of QCLs has rapidly improved over the last two decades, reaching a record output power of 5.1 W (8.3 W peak) and a 21% (27%) wall-plug efficiency (WPE) in continuous wave (pulsed mode) operation at room temperature [4]. Accelerated aging experiments have also established the reliable long-term operation of QCLs with an average power of 200 mW [9]. Tremendous progress has also been made in terms of achieving precise mode control and spectral tuning, which are critical for spectroscopic applications [10]. However, further advancement in the capabilities of compact QCL chips is highly desirable to meet the requirements of many emerging applications. This includes increasing the output power and

producing a single-mode, multi-wavelength output while reducing the footprint and/or costs of QCL sources.

Wavelength beam combining (WBC) offers a simple and effective way to achieve broadly tunable sources that are well-suited for high-speed hyperspectral imaging, for example, and chemical sensing. Moreover, WBC can be implemented to scale the overall power by merging the outputs from the QCL arrays into a single beam for applications that do not require a single-wavelength source. Previous studies have demonstrated the feasibility of WBC using free-space optics and showcasing, for example, their potential to boost power [11–14] and the usefulness of the approach for hyperspectral remote sensing [15]. With the emergence of photonic integrated circuits (PICs), there has been a significant push to leverage this new technology for the transition from bulky beam-combined laser sources to compact chip-scale devices.

Silicon photonics, owing to its low-cost structure, low-loss waveguides [16] and compact components, have emerged as market leaders for integrated photonic devices [17]. As a result, most mid-infrared on-chip WBC elements, such as Echelle or arrayed waveguide gratings (AWG) [18], have been developed to date on either silicon-on-insulator (SOI) [19–21] or germanium-on-silicon platforms [22]. However, this approach requires the integration of III-V semiconductor lasers with silicon platforms, which is challenging. While the majority of commercially available devices still rely on fiber coupling of the lasers to the silicon photonic chips, which requires additional connections [23], the integration of III-V diode lasers through hybrid [24], heterogeneous [25], and monolithic approaches [26] has steadily matured over the years.

Hybrid integration is yet to be explored beyond the $2\,\mu m$ wavelength [18], and the monolithic growth of QCL layers onto Si substrates involves complex growth strategies owing to the lattice mismatch and the difference in thermal expansion coefficients between III-V materials and silicon. However, heterogeneous integration successfully demonstrated high-brightness QCLs through WBC facilitated by AWGs [27,28]. Nevertheless, the output power levels were only a few milliwatts owing to the poor heat extraction and low transmission of III-V/Si evanescent tapers.

To overcome the challenge of producing a high-performance integrated WBC QCL source, a shift to an all-III-V monolithic semiconductor chip with integrated active and passive components was proposed [27]. The integration of low-loss passive III-V semiconductor waveguides with active QCLs has been studied [29] and achieved power outputs of $50\,mW$ and $880\,mW$ in continuous wave and pulsed operation, respectively, at room temperature [30]. Our recent work on high-efficiency AWGs fabricated on III-V semiconductor substrates demonstrated comparable performance to their silicon counterparts, making them suitable for WBC through an active/passive integration approach [31].

In this report, we present the first experimental demonstration of a monolithic closed-loop WBC QCL source. The chip comprises five QCL gain sections connected to 5×1 arrayed waveguide gratings (AWG) via tapered couplers and a router, as shown in Fig. 1(a). The QCL gain medium is used as the waveguide core in the passive portion of the chip, which undergoes ion implantation to reduce optical losses due to free carrier and intersubband absorption, as proposed by Montoya *et al.* [32] and in Ref. [33]. This approach avoids the additional etch and regrowth step or evanescent active/passive coupling schemes required by the previous methods [29,30] for obtaining low-loss waveguides. In addition to its beam-combining functionality, the AWG acts as a wavelength-selective optical filter, ensuring that each laser ridge locks its emission wavelength to its corresponding input channel. Our WBC chips operate at wavelengths close to $4.9\,\mu m$, producing peaks with a narrow linewidth of $2.4\,nm$ ($0.98\,cm^{-1}$/ $30\,GHz$) and $27\,dB$ side mode suppression ratio (SMSR). In pulsed mode, the peak power measured from the common aperture reaches $0.6\,W$ for each QCL array element.
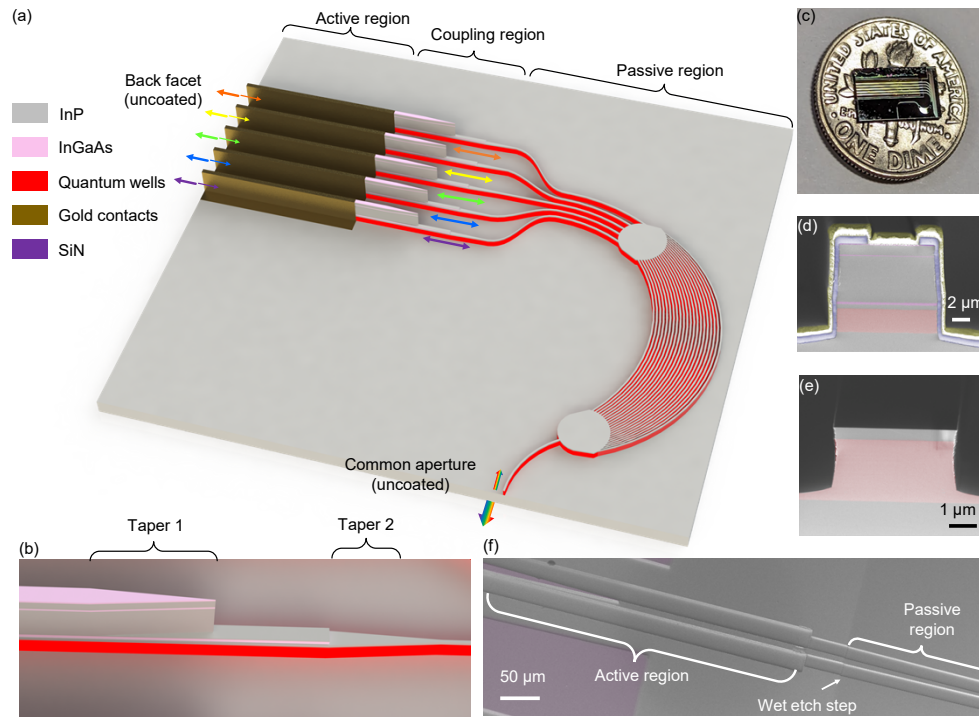
Fig. 1. (a) Schematic of a monolithic wavelength beam combined chip with five QCL gain sections integrated with an arrayed waveguide grating (AWG) to generate high-power multi-wavelength emission around λ ≈ 4.92 μm. (b) Magnified view of the coupling regions featuring two linear tapers in the upper cladding and waveguide core. Some of the dimensions are exaggerated for clarity. (c) Size comparison of the fabricated chip against a U.S. one-dime coin. (d) SEM cross-section of the active QCL gain medium ridge with false colors added to highlight different materials in the stack. (e) SEM cross-section of the passive ion-implanted region with false colors added to highlight the core material. (f) SEM top view of the coupling region for active to passive transition with marked etch step obtained after wet etching.

2. Methods

2.1. Design

The core of the base material used to fabricate our WBC QCL arrays is a strain-compensated InAlAs/InGaAs gain medium with 48 periods designed for emission around 4.85 μm. The band structure is based on a non-resonant extraction design similar to that described in [34]. A detailed description of the different layers comprising the top and bottom cladding is provided in Table 1.

As illustrated in Fig. 1(d) and (e), the ridge waveguides fabricated in the active (i.e., array of gain sections) and passive (i.e., low-loss router and AWG) portions of the WBC chips have significantly different geometries, although they share the QCL gain medium as the same core material. As discussed in detail in [30,31], this choice enables coupling between the passive/active sections with low insertion loss and greatly simplifies the processing because a regrowth step is not required, unlike for butt-coupled waveguides. However, ion implantation is required to reduce the material losses associated with free carriers and intersubband absorption. The electrically pumped ridges had a thicker top cladding and were wider (9.5 μm) to minimize the overlap of the laser mode with the lossy metal contacts. The length of the gain section was chosen to be ~ 6.9

Table 1. Stack profile of the QCL wafer

Layer	Material	Thickness (nm)	Doping (cm^{-3})
Contact layer	InGaAs	20	2×10^{19}
Contact layer/plasmon layer	InP	800	6×10^{18}
Etch stop layer	InGaAs	20	3×10^{16}
Top cladding	InP	1500	5×10^{16}
Top cladding	InP	2000	2×10^{16}
Etch stop layer	InGaAs	200	3×10^{16}
Spacer	InP	400	2×10^{16}
Gain medium	InGaAs/InAlAs	2016	(Injector sheet carrier density cm^{-2}) 1.16×10^{11}
Bottom cladding	InP	2500	2×10^{16}
Bottom cladding	InP	2500	5×10^{16}
Substrate	InP	-	3×10^{18}

mm, to ensure sufficient optical gain to reach the threshold and obtain a high peak power. In the passive section, the waveguide is significantly narrower (4.9 μm), and the top cladding consists only of a 0.4 μm thick InP layer for three main reasons: (1) to ensure a single TM mode operation, (2) to facilitate dry etching, especially in areas of the AWG where ridges are very close to each other, and (3) to minimize the implantation energy needed to reach depths over which material losses need to be reduced.

Considering the relatively low index contrast (0.1515) between gain medium (3.2348) and InP (3.0834), it was crucial to avoid significant bending losses. Thus, a minimum bending radius of 700 μm was used when designing the router and the AWG elements of the passive WBC PIC, resulting in radiation and mode-mismatch losses of less than 0.05 dB as shown in Fig. 2(a). We did not increase the bend radius beyond 700 μm to reduce the overall scattering losses, which were not accounted for in the simulations.
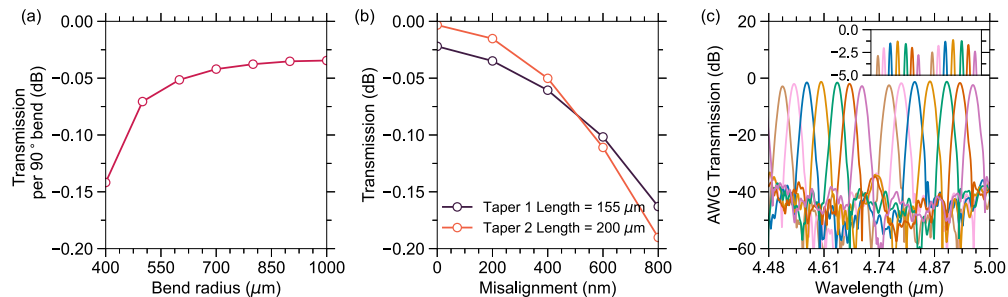
Fig. 2. Simulated plot of (a) transmission per 90-degree circular bend vs. bend radius, (b) misalignment tolerance of the linear tapers with the laser in the lateral direction, (c) simulated transmission of the 7×1 AWG vs. input wavelength for two different diffraction orders with inset depicting the maximum channel transmission.

As depicted in Fig. 1(b) and (f), a two-step coupler with two linear tapers was designed using the commercial Lumerical MODE package to minimize the insertion losses from the laser ridge to the passive waveguide. A first taper is used to accommodate the difference in the top cladding thickness between the ridge geometries, that is, the top ~4.5 μm from the upper cladding is gradually reduced to a point over a 155 μm length. A second tapered section is then implemented to narrow the waveguide width from 9.5 μm to 4.9 μm over a distance of 200 μm, as shown in

Fig. 1. According to our eigenmode expansion (EME) simulations, the insertion losses were lower than 0.025 dB for the chosen taper lengths and geometry. It is also important to consider any misalignment of the tapers to the laser ridges during fabrication, as shown in Fig. 2(b).

We designed the AWG with confocal star couplers according to the principles proposed by Smit *et al.* [18], which were followed in our previous work [31]. The key design parameters and characteristics of AWG are listed in Table 2. We designed two extra input channels not coupled to the laser ridges to verify the WBC operation with an external optical source, if needed. Hence, the central wavelength was assigned to the second input channel connected to the laser ridge instead of the third channel. The AWG transmission was obtained by Lumerical varFDTD simulation for the mth and $(m-1)^{th}$ diffraction orders, as shown in Fig. 2(c). The simulated peak positions deviate from the design values because of the 2.5-D nature of the simulation instead of being a full 3-D FDTD. Nevertheless, the experimentally determined channel spacing and free spectral range (FSR) agree very well with our model, as discussed later. Without accounting for waveguide propagation and bending losses, our simulations estimated a 1.1 dB insertion loss and 1.4 dB non-uniformity for the set of peaks centered at 4.92 μm wavelength.

Table 2. Design parameters of the AWG

Number of input channels	5
Number of arrayed waveguides	37
Star coupler length	200 μm
Arrayed waveguides center-to-center pitch at star coupler	5.1 μm
Arrayed waveguide length increment	26.62 μm
Star coupler tilt angle	31°
Input channel spacing at star coupler (1→5)	9.16; 8.22; 7.75; 7.36 μm
AWG channels, m^{th} order (1→5)	4.587; 4.626; 4.661; 4.692; 4.72 μm
AWG channels, $(m-1)^{th}$ order (1→5)	4.842; 4.882; 4.919; 4.952; 4.983 μm
Approximate footprint	1.53 mm^2

2.2. Fabrication

The QCL layers were grown via molecular beam epitaxy (MBE) on a conducting Si-doped InP wafer. The upper and lower cladding layers have low doping levels to minimize losses owing to free-carrier absorption. The fabrication of the WBC arrays started with two dry etching steps to create the ridges forming the gain sections, taper #1 in the top cladding, and define a large area for the passive WBC elements. This first phase required the deposition of multiple hard mask layers using plasma-enhanced chemical vapor deposition (PECVD), which was then patterned using standard photolithography (AZ3312 resist, Heidelberg MLA-150 exposure, AZ300 MIF developer), followed by an Ar/SF$_6$ reactive ion etching (RIE) step. The III-V material was subsequently etched using inductively coupled (ICP) RIE (SAMCO-200iP) at a high-temperature (250 °C) process based on Ar/BCl$_3$/SiCl$_4$ gases. Alignment of taper #1 to the laser ridge was performed using the standard MLA-150 alignment procedure. The passive region was simultaneously etched down through most of the top InP cladding layer.

Because of the poor selectivity of our RIE recipe between InP and InGaAs, HCl:H$_2$O (1:1) and H$_2$SO$_4$:H$_2$O$_2$:H$_2$O (1:1:40) solutions were then used to selectively etch any InP and the 200 nm InGaAs layer remaining on top of the 400 nm thick InP spacer above the QCL gain region. This process resulted in a ~500 nm step in the waveguide, as shown in Fig. 1(f). According to our eigenmode expansion (EME) simulations, the insertion loss associated with this discontinuity was less than 0.2 dB.

The second taper, narrowing the ridges from 9.5 µm down to 4.9 µm, the passive waveguides forming the router, and the AWG structure were later fabricated simultaneously using e-beam lithography (Elionix F-125) and dry etching, following the established protocols described in [31]. Figure 1(b) depicts the entire coupler region, which transitions from the active region of the chip to the passive region. A 600 nm nitride layer was then deposited by PECVD and patterned to cover only the gain sections, leaving a narrow opening on top of these ridges to allow the electrical connection. The passive regions, including the couplers, were then ion-implanted with protons to lower material losses, especially those originating from the unpumped QCL gain medium. An 8-step implantation recipe with energies ranging from 45 to 600 keV and an average dose of 5×10^{13} /cm^2 was used. The areas where ion implantation was not desired were protected by a photoresist layer that was at least 20 µm thick.

Finally, individual electrical contacts were created for each gain section by sputtering and patterning a thick Ti/NiV/Au stack. The same metal layers were deposited on the back of the substrate to act as ground electrodes. After fabrication, the chips were cleaved to expose the waveguide facets at the common AWG output and at the back of the five laser ridges, which act as mirrors for the AWG coupled Fabry-Perot (FP) laser.

2.3. Measurement and analysis

The laser spectra were measured by electrically pumping each laser ridge individually in pulsed mode using custom drive electronics. The pulse width was typically 300 ns, and the repetition rate was maintained between 5 and 30 kHz. For spectral measurements, the laser beam emanating from either the common output waveguide or the back facet was collimated using an f/1 AR-coated CaF$_2$ lens and analyzed using a Bruker Fourier transform infrared (FTIR) spectrometer equipped with a deuterated triglycine sulfate (DTGS) detector. A calibrated thermopile power meter is used to measure the laser output power. The QCL chip was pressed against a copper heatsink connected to a thermoelectric cooler (TEC). The latter maintained the copper mount temperature at 25 °C for the duration of all measurements, unless specified otherwise.

The optical losses incurred in various passive elements were inferred by cleaving the chip several times and measuring the laser output power versus current data after each step, as discussed in Section 3.2. The total losses in the WBC chip can be divided into five terms: the propagation losses in the active and passive waveguides over their respective lengths (that is, $\alpha_{active} \cdot L_{active}$ and $\alpha_{passive} \cdot L_{passive}$), transmission through the active-to-passive coupler ($T_{coupler}$), AWG (T_{AWG}), and mirror losses. The dependence of the threshold current density (j_{th}) on the total optical loss is given by:

$$j_{th} = \frac{\alpha_{active}.L_{active} + \alpha_{passive}.L_{passive} + \ln\left(\frac{1}{T_{coupler}}\right) + \ln\left(\frac{1}{T_{AWG}}\right) + \ln\left(\frac{1}{r_1 \cdot r_2}\right)}{\Gamma.g.L_{active}} + j_{tr} \tag{1}$$

where Γ is the gain overlap factor; g is the gain coefficient per cascade; r_1 and r_2 are the amplitude reflectivities of the front and back facets, respectively; and j_{tr} is the transparency current density of the gain medium. The values of $\Gamma \cdot g$ and j_{tr} were previously determined using the inverse cavity length experimental method described in [35]. The first four loss terms can be estimated sequentially by measuring the threshold current density after each cleave and comparing the results obtained with the values calculated using Eq. (1).

3. Results and discussion

3.1. Laser spectra and power characteristics

The emission spectra of the five array elements of a representative WBC QCL chip are presented in Figs. 3(a)–(d). Figures 3(a) and 3(c) illustrate the spectra measured from the common output waveguide, whereas Figs. 3(b) and 3(d) correspond to the spectra emitted from the back facet

of each laser ridge. When the drive current is close to the threshold, each laser emits a single and well-defined peak aligned accurately with a different input channel of the AWG. This was expected because the AWG acted as an optical filter integrated within the laser cavity formed by the two cleaved end facets. The laser emission is located at wavelengths corresponding to the (m-1)th AWG order mentioned in Table 2 because at low voltages, the gain of the QCL has its maximum near 4.85 μm. As the current increased and approached the rollover point, the gain spectrum experienced a blue shift, as shown by the luminescence data presented in Fig. 3. Consequently, narrow secondary peaks that closely align with the AWG wavelengths from the lower AWG order appear in the emission spectra of lasers #4 and #5. Several broad and low-intensity features consisting of many FP modes can also be observed at high currents but only in the spectra from the back facet. These parasitic FP modes do not have a consistent free spectral range, and are thus likely due to minor fabrication defects in the coupling regions or along the length of the passive waveguides, leading to additional reflections/feedback into the laser cavities. Nevertheless, the spectra obtained from the common output waveguide consist only of narrow peaks selected by the AWG. These experimental findings provide compelling evidence that the AWG structure controls the optical feedback into the gain medium and, consequently, the selected laser wavelengths, demonstrating that on-chip WBC are achieved.

Figures 3(e) and (f) show the laser power measured from the common output and back facet, respectively. For the common output facet, more than 0.7 W of peak power is achieved for lasers 4 and 5 with no apparent saturation, whereas for lasers 1, 2, and 3, the intensity reaches a plateau around 0.6 W. This difference can be traced back to the emergence of secondary peaks related to the AWG in the emission spectra of lasers 4 and 5 at high currents. Hence, we conclude that the mth order diffraction contributes the extra 0.1/0.2 W for lasers 4 and 5. In the case of the power measured from the back facet, none of the lasers showed saturation, and the peak power was close to 1 W. However, part of the power measured was a contribution from the low-intensity peaks shown in Fig. 3(d), which do not have the desired wavelengths and probably originate from fabrication defects in the coupler region or along the passive section of the WBC chips between the backfacet and the AWG. These defects scatter enough light back into the gain sections to allow lasing on modes not controlled by the AWG transmission. Note that the saturation effect observed in the data presented may be due to these undesirable modes, although other phenomena such as spatial hole burning and phase errors in the AWG may also play a role. We are currently investigating this subject and additional details will be given in a future publication.

Figure 4(a) shows the deviation between the emission wavelengths obtained experimentally at 25 °C and the AWG design values for five different WBC chips under similar driving conditions. Without active control, the measured values deviated by less than 5 nm (2 cm^{-1}) from the design. More precisely, the observed discrepancy had two components. First, the average wavelength for each AWG channel was systematically detuned by approximately 4% with respect to the designed value. This error is likely due to the finite accuracy with which the refractive indices of the different waveguide materials are known and their temperature dependence. Second, the spread in emission wavelengths, which is less than +/- 3 nm (~1.5 cm^{-1}), is random and likely related to fabrication errors such as non-uniformity in ridge width and etch depth across the chip. We expect that the systematic error observed can be significantly reduced by refining the input parameters used in our simulations and by using the data presented in Fig. 4(a) for calibration.

According to Fig. 4(b), the linewidth of one of the lasers measured varies between 0.5-0.98 cm^{-1} (15-30 GHz) as the current increases up to rollover. This occurred because of the low-quality factor (~400) of the AWG and the relatively long pulses (300 ns) used to drive our arrays. This is on one hand quite broad compared to the intrinsic linewidth of distributed-feedback (DFB) QCLs, but on the other hand relatively narrow compared to the chirp (3 to 10 cm^{-1}) experienced by DFB QCLs with similar geometry fabricated from the same material and operated under the same pulsed conditions. Additionally, the linewidth broadened by less than a factor of two as the pulse
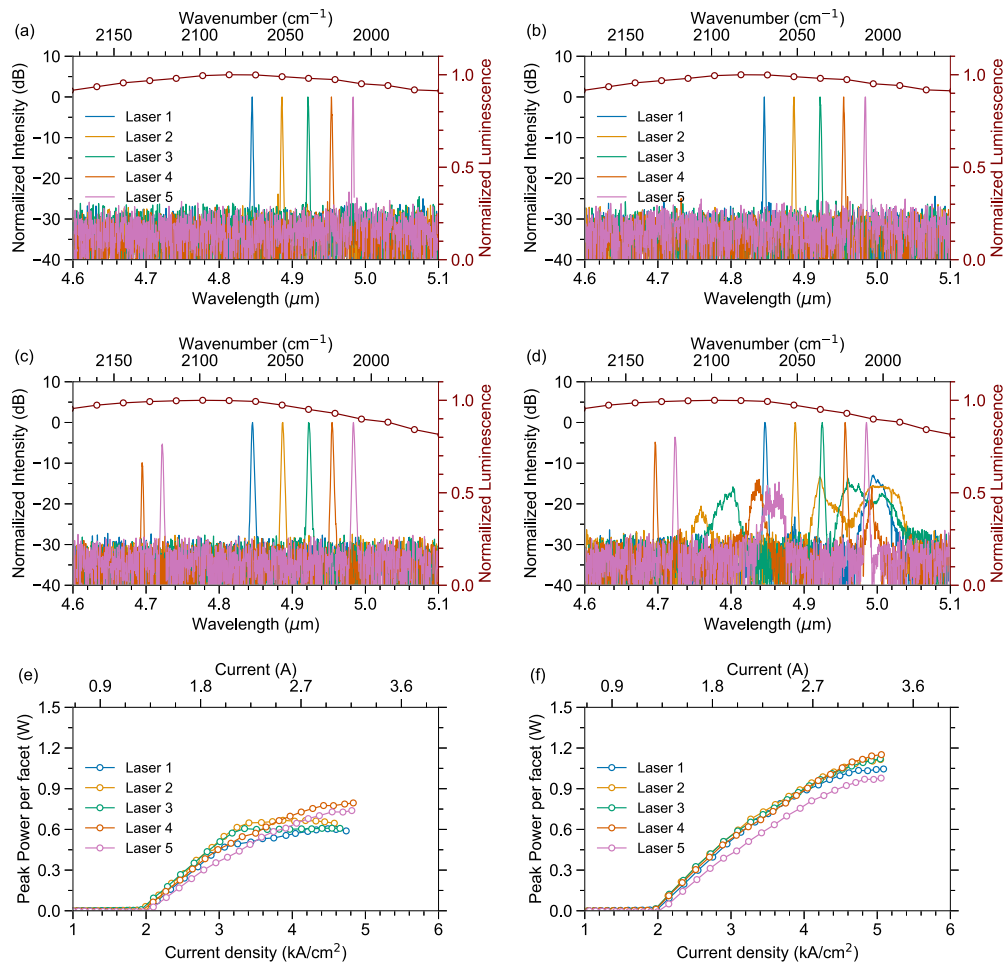
Fig. 3. Emission spectra obtained at room temperature of the WBC chip from (a) common output near threshold current, (b) back facet near threshold current, (c) common output waveguide near rollover current, (d) back facet near rollover current. The luminescence measured at the voltage as the laser data presented is also shown. Measured peak power vs. current density from (e) common output waveguide, (f) back facet. All the measurements were performed under pulsed operation (300 ns pulses, 30kHz repetition rate) at room temperature.

length increased beyond 1 µs. The SMSR remained above 27 dB in the spectra measured from the common output because the AWG efficiently blocked unwanted FP modes. The laser wavelength redshifts by less than 0.5 nm (0.22 cm^{-1}), as the current density increases from the threshold to the rollover. This weak wavelength dependence with current indicates that the AWG passive region remains mostly thermally insulated from the Joule heating that occurs in the electrically pumped ridges. The inset of Fig. 4(b) plots the laser peak on a linear scale and highlights that the line shape may result from the superposition of a few peaks. This is expected because of the multitude of FP modes supported by the cavity, which can lase owing to the relatively broad transmission of the AWG channels (full width at half maximum ~ 11 nm or ~7.5 cm^{-1}).

Figure 4(c) shows the shift in the output wavelength as a function of heatsink temperature. The AWG exhibited a linear temperature dependence for the selected wavelengths, as shown in
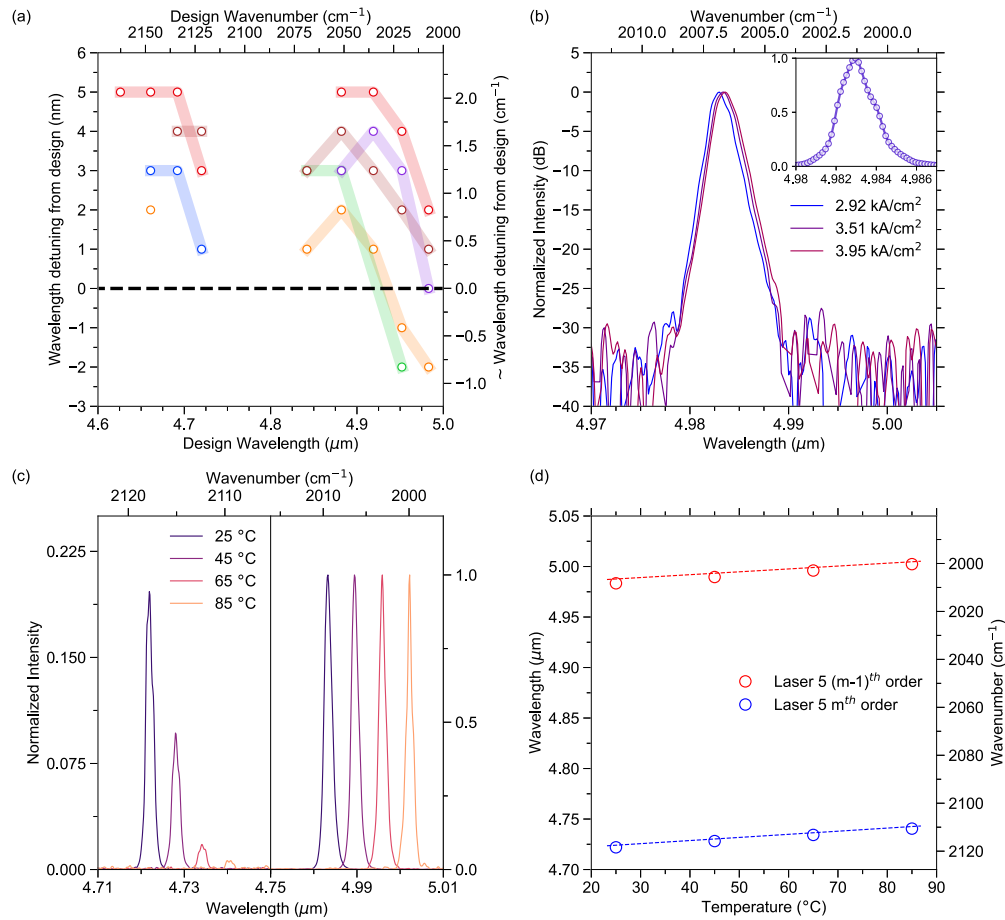
Fig. 4. (a) Deviation of measured wavelengths with respect to the AWG design values for both mth and (m-1)th diffraction orders. Different colors are used to represent data obtained from different chips. (b) (m-1)th order peak of laser 5 for increasing current densities on a logarithmic scale. The same data plotted on a linear scale is shown in the inset. (c) Peak position shift of the mth (left) and (m-1)th (right) order for laser 5 with increasing heatsink temperature. Each spectrum was normalized with respect to the maximum intensity of the (m-1)th order peak. (d) Linear fit for peak positions vs. temperature values calculated from (c).

Fig. 4(d), with slopes of 0.1376 cm^{-1}/K and 0.1271 cm^{-1}/K for the mth and (m-1)th diffraction order for laser 5. The former value is close to the temperature tuning coefficient (0.142 cm^{-1}/K) of λ~4.65 µm, 9.5 µm wide DFB QCLs fabricated from the same wafer. Hence, our monolithic WBC chip can achieve a wavelength tunability of approximately 5 cm^{-1} by varying the temperature by 40 K.

3.2. Performance comparison between Fabry-Perot QCLs and WBC chips

To determine the optical losses in different parts of our WBC chips, we measured the laser characteristics of a few samples after cleaving them at three different positions, as shown in Fig. 5(a). Figures 5(b) and (c) depict how the output power varies after each cleave in the case of a representative array element. This correlates with the contribution of each section to

absorption/scattering losses in the cavity. We observe that most of the losses are incurred in the AWG and the long passive waveguide section, that is, after the first cleave.
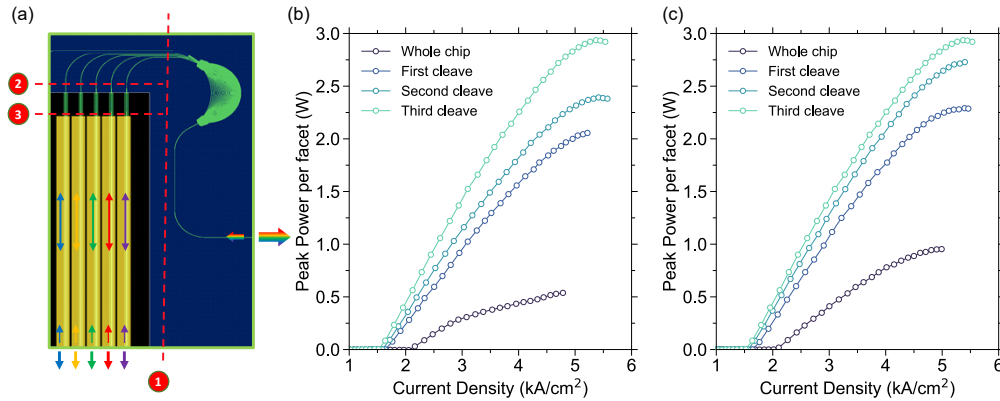
Fig. 5. (a) Schematic of the WBC chip with red dotted lines marking the position of each cleave done to estimate the losses originating from various sections on the chip. Measured peak power vs. current density from (b) common output waveguide/front facet and (c) back facet for a representative laser element.

By measuring the threshold current density after each cleave and comparing the results obtained with the values calculated using Eqs. (1), we estimated the optical losses listed in Table 3. The transmission of AWG channel #1 could not be calculated, because the corresponding lasers suffered from electrical shorts. Also, the value of j_{tr}, and $\Gamma \cdot g$ used in our calculations came from a previous experiment that yielded $0.52 \, \text{kA/cm}^2$ and $3.06 \, \text{cm}^{-1}/\text{kA}$ respectively. The reflectivities of the front and back facets were simulated to be approximately 0.235 and 0.245, respectively.

Table 3. Optical losses in various elements

Measured property	Experimental value	Simulation
α_{active}	$3.69 \pm 0.62 \, \text{dB/cm}$	-
Coupler Loss	$0.90 \pm 0.47 \, \text{dB}$	$< 0.225 \, \text{dB}$
$\alpha_{passive}$	$3.16 \pm 0.64 \, \text{dB/cm}$	-
AWG channel 2 loss	$1.66 \pm 0.30 \, \text{dB}$	$1.10 \, \text{dB}$
AWG channel 3 loss	$1.85 \pm 0.30 \, \text{dB}$	$1.22 \, \text{dB}$
AWG channel 4 loss	$2.62 \pm 0.60 \, \text{dB}$	$1.65 \, \text{dB}$
AWG channel 5 loss	$3.82 \pm 0.75 \, \text{dB}$	$2.40 \, \text{dB}$

The results presented in Table 3 were obtained by measuring three independent WBC chips, and were generally larger than the predictions of our models. Although the discrepancy between the results of our simulations and our experiment is notable, the information collected and presented in Table 3 allows us to identify critical areas that need improvement. The performance and overall beam combining efficiency of our WBC chips can be drastically improved, for example, by implementing AWGs with higher transmission, minimizing the number of fabrication defects, and reducing waveguide propagation losses. The use of wet etching to smoothen the sidewall roughness is a possible solution to achieve better performance [36]. With further loss mitigation, the current results pave the way toward accomplishing on-chip WBC in the mid-IR without significantly compromising the QCL power levels.

4. Conclusion

In this study, we discussed the design, fabrication, and characterization of monolithic closed-loop WBC QCL arrays using AWGs as integrated beam-combining elements. We demonstrated that the AWG could select the lasing wavelength of each array element by controlling the feedback to the gain medium. Power levels reaching 0.6 W per laser were achieved from the common output facet, and optimizing the laser parameters such as the length of the active region and the mirror reflectivity by adding anti-reflection/high-reflection coatings can achieve even higher power levels. Moreover, waveguide losses can be reduced significantly by minimizing fabrication defects, improving the alignment accuracy of the different lithography steps, and readjusting the central wavelength of the AWG to better match the gain maximum. This will bring the performance of our monolithic WBC arrays closer to the power and WPE achievable with standalone FP QCL lasers. The present results represent a key step toward the development of compact, low-cost, and beam-combined mid-infrared QCL sources.

Disclosures. The authors declare no conflicts of interest.

Data availability. Data underlying the results presented in this paper are not publicly available at this time but may be obtained from the authors upon reasonable request.

References

1. Y.-J. Shen, B.-Q. Yao, X.-M. Duan, *et al.*, "103 W in-band dual-end-pumped Ho:YAG laser," Opt. Lett. **37**(17), 3558–3560 (2012).
2. C. Wang, Y. Niu, S. Du, *et al.*, "High-power diode-side-pumped rod Tm:YAG laser at 2.07 μm," Appl. Opt. **52**(31), 7494–7497 (2013).
3. G. Belenky, L. Shterengas, G. Kipshidze, *et al.*, "Type-I Diode Lasers for Spectral Region Above 3 μm," IEEE J. Sel. Top. Quantum Electron. **17**(5), 1426–1434 (2011).
4. Y. Bai, N. Bandyopadhyay, S. Tsao, *et al.*, "Room temperature quantum cascade lasers with 27% wall plug efficiency," Appl Phys Lett **98**(18), 181102 (2011).
5. I. Vurgaftman, C. L. Canedy, C. S. Kim, *et al.*, "Mid-infrared interband cascade lasers operating at ambient temperatures," New J. Phys. **11**(12), 125015 (2009).
6. W. R. Bosenberg, A. Drobshoff, J. I. Alexander L, *et al.*, "93% pump depletion, 35-W continuous-wave, singly resonant optical parametric oscillator," Opt. Lett. **21**(17), 1336–1338 (1996).
7. L. E. Myers, R. C. Eckardt, M. M. Fejer, *et al.*, "Quasi-phase-matched optical parametric oscillators in bulk periodically poled LiNbO₃," J. Opt. Soc. Am. B **12**(11), 2102–2116 (1995).
8. J. Faist, F. Capasso, D. L. Sivco, *et al.*, "Quantum Cascade Laser," Science **264**(5158), 553–556 (1994).
9. F. Xie, H. K. Nguyen, H. Leblanc, *et al.*, "Long term reliability study and life time model of quantum cascade lasers," Appl Phys Lett **109**(12), 121111 (2016).
10. M. Shahmohammadi, F. Kapsalidis, M. J. Süess, *et al.*, "Multi-wavelength distributed feedback quantum cascade lasers for broadband trace gas spectroscopy," Semicond. Sci. Technol. **34**(8), 083001 (2019).
11. B. G. Lee, J. Kansky, A. K. Goyal, *et al.*, "Beam combining of quantum cascade laser arrays," Opt. Express **17**(18), 16216–16224 (2009).
12. S. Hugger, R. Aidam, W. Bronner, *et al.*, "Power scaling of quantum cascade lasers via multiemitter beam combining," Opt. Eng. **49**(11), 111111 (2010).
13. T. Y. Fan, "Laser beam combining for high-power, high-radiance sources," IEEE J. Sel. Top. Quantum Electron. **11**(3), 567–577 (2005).
14. R. K. Huang, B. Chann, J. Burgess, *et al.*, eds. Proc. SPIE 97300C, 1–9 (2016).
15. A. Goyal, T. Myers, C. A. Wang, *et al.*, "Active hyperspectral imaging using a quantum cascade laser (QCL) array and digital-pixel focal plane array (DFPA) camera," Opt. Express **22**(12), 14392–14401 (2014).
16. S. A. Miller, M. Yu, X. Ji, *et al.*, "Low-loss silicon platform for broadband mid-infrared photonics," Optica **4**(7), 707–712 (2017).
17. N. Margalit, C. Xiang, S. M. Bowers, *et al.*, "Perspective on the future of silicon photonics and electronics," Appl Phys Lett **118**(22), 220501 (2021).
18. M. K. Smit and C. Van Dam, "PHASAR-based WDM-devices: Principles, design and applications," IEEE J. Select. Topics Quantum Electron. **2**(2), 236–250 (1996).

19. A. Malik, A. Spott, A. Spott, *et al.*, "High resolution, high channel count mid-infrared arrayed waveguide gratings in silicon," Opt. Lett. **45**(16), 4551–4554 (2020).
20. A. Malik, M. Muneeb, S. Radosavljevic, *et al.*, "Silicon-based Photonic Integrated Circuits for the Mid-infrared," Procedia Eng **140**, 144–151 (2016).
21. M. Muneeb, X. Chen, P. Verheyen, *et al.*, "Demonstration of Silicon-on-insulator mid-infrared spectrometers operating at 3.8μm," Opt. Express **21**(10), 11659–11669 (2013).
22. A. Malik, E. J. Stanton, J. Liu, *et al.*, "High Performance 7 × 8 Ge-on-Si Arrayed Waveguide Gratings for the Midinfrared," IEEE J. Sel. Top. Quantum Electron. **24**(6), 1–8 (2018).
23. L. Ranno, P. Gupta, K. Gradkowski, *et al.*, "Integrated Photonics Packaging: Challenges and Opportunities," ACS Photonics **9**(11), 3467–3485 (2022).
24. S. Zeng, X. Zhao, Y. Zhu, *et al.*, "Watt-level beam combined diode laser systems in a chip-scale hybrid photonic platform," Opt. Express **30**(13), 23815–23827 (2022).
25. A. Spott, J. Peters, M. L. Davenport, *et al.*, "Quantum cascade laser on silicon," Optica **3**(5), 545–551 (2016).
26. H. Nguyen-Van, A. N. Baranov, Z. Loghmari, *et al.*, "Quantum cascade lasers grown on silicon," Sci. Rep. **8**(1), 7206 (2018).
27. J. X. B. Sia, W. Wang, Z. Qiao, *et al.*, "Compact silicon photonic hybrid ring external cavity (SHREC)/InGaSb-AlGaAsSb wavelength-tunable laser diode operating from 1881-1947 nm," Opt. Express **28**(4), 5134–5146 (2020).
28. E. J. Stanton, A. Spott, J. Peters, *et al.*, "Multi-spectral quantum cascade lasers on silicon with integrated multiplexers," Photonics **6**(1), 6 (2019).
29. S. Jung, D. Palaferri, K. Zhang, *et al.*, "Homogeneous photonic integration of mid-infrared quantum cascade lasers with low-loss passive waveguides on an InP platform," Optica **6**(8), 1023–1030 (2019).
30. R. Wang, P. Täschler, Z. Wang, *et al.*, "Monolithic Integration of Mid-Infrared Quantum Cascade Lasers and Frequency Combs with Passive Waveguides," ACS Photonics **9**(2), 426–431 (2022).
31. T. S. Karnik, K. P. Dao, Q. Du, *et al.*, "High-efficiency mid-infrared InGaAs/InP arrayed waveguide gratings," Opt. Express **31**(3), 5056–5068 (2023).
32. J. Montoya, C. Wang, A. Goyal, *et al.*, "Integration of quantum cascade lasers and passive waveguides," Appl. Phys. Lett. **107**(3), 1 (2015).
33. A.K. Goyal, "Photonic integrated circuits based on quantum cascade structures," US Patent 9,450,053 B2 (20 Sep. 2016).
34. A. Lyakh, R. Maulini, A. Tsekoun, *et al.*, "3 W continuous-wave room temperature single-facet emission from quantum cascade lasers based on nonresonant extraction design approach," Appl. Phys. Lett. **95**(14), 1 (2009).
35. J. S. Yu, S. Slivken, A. J. Evans, *et al.*, "High-performance continuous-wave operation of λ ∼ 4.6 μm quantum-cascade lasers above room temperature," IEEE J. Quantum Electron. **44**(8), 747–754 (2008).
36. K. Zhang, G. Böhm, and M. A. Belkin, "Mid-infrared microring resonators and optical waveguides on an InP platform," Appl. Phys. Lett. **120**(6), 061106 (2022).